Evaluating the fractal dimension of profiles

B. Dubuc
McGill Research Center for Intelligent Machines, McGill University, 3480 University Street, Montréal, Québec, Canada H3A 2A7

J. F. Quiniou and C. Roques-Carmes
Laboratoire de Microanalyse des Surfaces, ENSMM, Route de Gray, 25030 Besançon Cédex, France

C. Tricot
Departement de Mathématiques Appliquées, Ecole Polytechnique, Université de Montréal, Case Postale 6079, Succursale A, Montréal, Québec, Canada, H3C 3A7

S. W. Zucker
Canadian Institute for Advanced Research and McGill Research Center for Intelligent Machines, McGill University, 3480 University Street, Montréal, Québec, Canada H3A 2A7

(Received 11 May 1988)

There are many definitions of the fractal dimension of an object, including box dimension, Bouligand-Minkowski dimension, and intersection dimension. Although they are all equivalent in the continuous domain, they differ substantially when discretized and applied to digitized data. We show that the standard implementations of these definitions on self-affine curves with known fractal dimension (Weierstrass-Mandelbrot, Kiesswetter, fractional Brownian motion) yield results with significant errors. An analysis of the source of these errors leads to a new algorithm in one dimension, called the variation method, which yields accurate results. The variation method uses the notion of ϵ oscillation to measure the amplitude of the one-dimensional function in an ϵ neighborhood. The order of growth of the integral of the ϵ oscillation (called the ϵ variation), as ϵ tends toward zero, is directly related to the fractal dimension. In this paper, we present the variation method for one-dimensional (1D) profiles and show that, in the limit, it is equivalent to the classical box-counting method. The result is an algorithm for reliably estimating the fractal dimension of 1D profiles; i.e., graphs of functions of a single variable. The algorithm is tested on profiles with known fractal dimension.

I. INTRODUCTION

Points, segments, and disks have fractal dimension 0, 1, and 2, respectively. But in between those objects with integer dimensions lie complex, irregular objects whose fractal dimension can be thought of as a measure of their irregularity. The fractal dimension of a curve, for instance, will lie between 1 and 2, depending on how much area it fills (Fig. 1). The same idea can be extended to surfaces, but this time with the fractal dimension lying between 2 and 3. The fractal dimension can thus be used to compare the complexity of two curves or two surfaces, and therein lies its importance for applications. In materials science, e.g., the fractal dimensions is directly related to roughness,[1] and it finds basic applications in stereology,[2] powder technology,[3,4] geology,[5] metallurgy,[6] computer vision,[7–9] and so on. But from a computational perspective, there are many definitions of fractal dimension. Although most of them are equivalent in the continuous domain, when discretized and applied to digitized data they lead to different algorithms and different results. Which of these algorithms is the most robust? Do they properly distinguish between fractal and nonfractal objects? The answers are not known. As a step toward them, in this paper we compare their performance on mathematical objects with known fractal dimension. These mathematical objects thus provide a kind of "backdrop" or "benchmark," and on this basis we show that the standard algorithms often exhibit errors of 10–20%. But most importantly, further analysis of the problems with the standard algorithms leads us to a new type of algorithm for estimating fractal dimension that is significantly more accurate.

This paper is the first of series of two, and it concentrates on the study of curves or one-dimensional (1D) profiles. Our goal is to develop an algorithm that provides accurate results, that is efficient to run, and that can be generalized to the study of higher-dimensional profiles. In another paper,[10] we carry out this generalization, and illustrate its application to the study of rough surfaces.

The paper is organized as follows. In Sec. II we review the definitions of fractal dimension that are the most widely used, and in Sec. III present the algorithms derived from those definitions. To evaluate their accuracy, all algorithms are applied to the evaluation of the fractal dimension of known theoretical models, in particular, Weierstrass-Mandelbrot curves and Brownian motion, two classical fractals. The weaknesses of those algorithms will be stressed. But the heart of the paper is Sec. IV, in which we present a new type of algorithm to evaluate the fractal dimension of graphs of functions. After developing a method based on horizontal structuring ele-

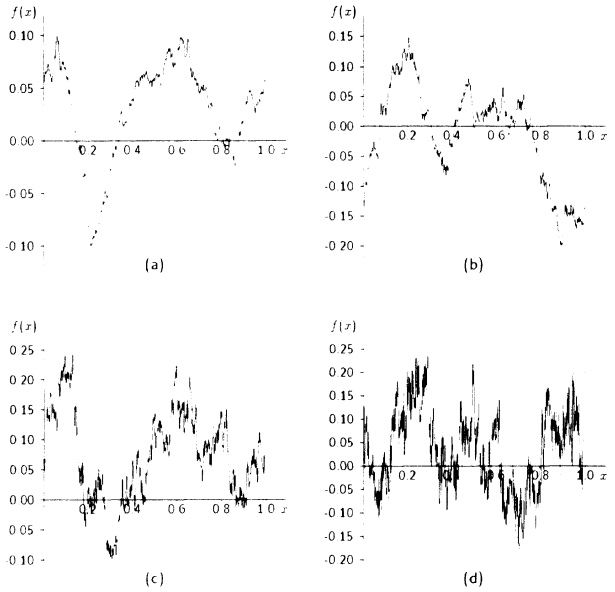

FIG. 1. Different curves with increasing fractal dimension. In (a) the fractal dimension is 1.2, in (b) 1.4, (c) 1.6, and (d) 1.8. Note how the irregularity of the curve increases with dimension, as does the area which they fill.

ments, we refine it into a related but more efficient *variation method,* which uses the notion of ϵ oscillation to measure the amplitude of a one-dimensional function in an ϵ neighborhood. It is the rate of growth of the integral of the ϵ oscillation (which we call ϵ variation) that is directly related to the fractal dimension, and our algorithm for estimating this is shown to be a substantial improvement over the standard ones in two ways. First, the estimates of fractal dimension are more accurate; and second, the algorithm is much more efficient to implement. In fact, it provides the basis for our higher-dimensional algorithm.[10] A mathematical background reference for the variation method in $\mathbb{R}^2$ and for the horizontal structuring element method can be found in Tricot *et al.*[11]

A. Notation

Throughout this paper, we shall base our analysis on a function f of a real variable x, continuous on its domain of definition. This domain will be an interval, usually [0,1] [for the box-counting, *Minkowski covers,* and variation method] but also $[0,\infty)$ (for the power spectrum method). The assumption of continuity is crucial for the proofs of our results, and is relevant for modeling natural situations such as rugosimetric profiles. The graph of f is the plane set

$$G_f=\{(x,f(x)):\ x\in[0,1]\}\ .$$

Throughout this text, by the terms curve, profile, and 1D-profile, we shall refer to the graph of a function of a single variable. Our goal is to evaluate the fractal dimension of G_f, denoted $\Delta(G_f)$, from sample points.

II. BOXES, COVERINGS, AND FRACTAL DIMENSION

The most widely used definitions of dimension are the Minkowski-Bouligand dimension and the box dimension. Those are based on the pioneering studies by Bouligand,[12] and are described in Mandelbrot.[13] Although they are mathematically equivalent in the limit, in practice they give rise to algorithms that behave quite differently. The reason for this difference derives from the way that limits are taken, and the manner in which they approach zero. But there is a common aspect as well, which we collect into the notion of a generalized cover,[11] that is defined in the conclusion of this section to be used later on.

A. Minkowski-Bouligand dimension

The *Minkowski cover* of a set E is the set of all points $E(\epsilon)$ defined as follows:

$$E(\epsilon)=\{y:\ y\in B_\epsilon(x),\ x\in E\}\ ,$$

where $B_\epsilon(x)$ is a disk of radius ϵ centered on x. In other words, $E(\epsilon)$ consists in the union of all the disks centered on E, with radius ϵ (Fig. 2). Note that this definition of a covering differs from the standard mathematical usage in that it is the union of balls covering a set E instead of the family of balls whose union covers E. In the fractal literature such coverings sometimes have been referred to as "sausages."

Let $|S|_2$ denote the area of a region S in $\mathbb{R}^2$. The area of the Minkowski cover is then $|E(\epsilon)|_2$, and the Minkowski-Bouligand (MB) dimension for E is defined as follows:

$$\Delta_{\mathrm{MB}}(E)=\lim_{\epsilon\to 0}\left[2-\frac{\ln|E(\epsilon)|_2}{\ln\epsilon}\right]$$
$$=\inf\{\alpha:\ \epsilon^{\alpha-2}|E(\epsilon)|_2\xrightarrow[\epsilon\to 0]{}0\}\ , \qquad (1)$$

i.e., $\Delta_{\mathrm{MB}}(E)$ is the lower bound of all α such that $\epsilon^{\alpha-2}|E(\epsilon)|_2$ tends to 0 when ϵ itself tends to 0.

If we make the assumption that $\epsilon^{\alpha-2}|E(\epsilon)|_2$ does not

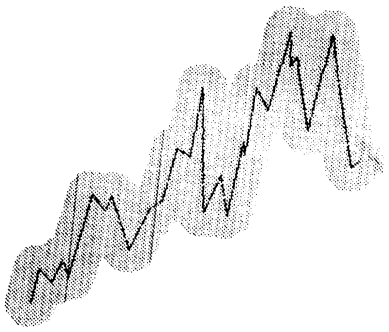

FIG. 2. Minkowski cover $E(\epsilon)$. The object E is in black. The shaded area represents the Minkowski cover $E(\epsilon)$ where ϵ represents 30 units inside a square window of 350 units (pixels). The pixels in gray in this image are the pixels that are at a distance to the curve less than or equal to 30 pixels (where the horizontal distance between two adjacent pixels is $\frac{1}{350}$).

depend on ϵ for $\alpha=\Delta_{MB}(E)$, we obtain a linear relationship

$$\ln\frac{1}{\epsilon^2}|E(\epsilon)|_2=\Delta_{MB}(E)\ln\frac{1}{\epsilon}+c \ ,$$

with c constant. In other words, $\Delta_{MB}(E)$ can be estimated by the slope of the log-log plot:

$$(\ln(1/\epsilon),\ \ln[(1/\epsilon^2)|E(\epsilon)|_2]) \ . \tag{2}$$

Such plots are typically used in practice, since a least-mean-square line can be fit to it to reduce quantization and other forms of error.

B. Box dimension

This definition is based upon a quantization of the space in which the curve is embedded. Define a decreasing sequence ϵ_k tending to 0 slowly, such as a geometric sequence (a sufficient condition is that the ratio $\ln\epsilon_k/\ln\epsilon_{k+1}$ tends toward 1). The set E can then be covered by a grid with pixel (i.e., picture element) length ϵ_k, and the number of pixels $\Omega(E,\epsilon_k)$ that intersect E can be counted (Fig. 3). More formally, the *box dimension* is given by

$$\Delta_B(E)=\lim_{k\to\infty}\frac{\ln\Omega(E,\epsilon_k)}{\ln(1/\epsilon_k)}$$
$$=\inf\{\alpha:\ \epsilon_k^{\alpha}\Omega(E,\epsilon_k)\xrightarrow[k\to\infty]{}0\} \ . \tag{3}$$

As in Sec. II A, an estimate of $\Delta_B(E)$ is given by the slope of the line passing through the points

$$(\ln(1/\epsilon_k),\ln\Omega(E,\epsilon_k)) \ . \tag{4}$$

We will show later that the Minkowski-Bouligand dimension and the box dimension are equivalent (see also Bouligand[12]). There are many other equivalent formulations as well, and we will introduce another one in Sec. II C. For the sake of simplicity, we will use a unique notation $\Delta(E)$, and refer to it as the fractal dimension of the set E. (Note that although the Minkowski-Bouligand and the box dimension are equivalent to each other, they may differ from the Hausdorff dimension.[14,15] In this paper we shall not consider the Hausdorff dimension.)

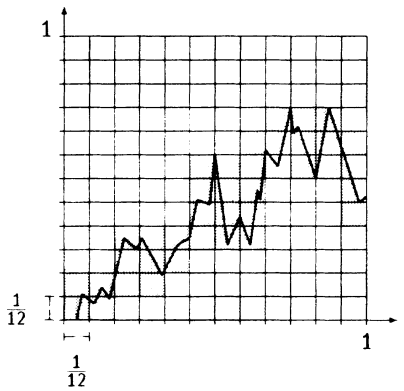

FIG 3. Definition of box dimension. The object E (dark curve) lies in the unit square which has been subdivided into 144 small boxes with side $\epsilon_k=\frac{1}{12}$. The boxes intersecting E are shaded. A count of the shaded boxes yields $\Omega(E,\epsilon_k)=38$ for $\epsilon_k=\frac{1}{12}$.

C. Dilation of profiles and generalized covers

A comparison of Figs. 2 and 3 suggests a common structure between them. We saw that for the box-counting method, the set E was covered by $\Omega(E,\epsilon_k)$ pixels with side ϵ_k. Let $U(\epsilon_k)$ denote the union of all those squares, and $|U(\epsilon_k)|_2$ denote the area of the special shaped cover. This area is equal to $\Omega(E,\epsilon_k)\epsilon_k^2$. The fractal dimension can then be written as

$$\Delta(E)=\lim_{k\to\infty}\left[2-\frac{\ln|U(\epsilon_k)|_2}{\ln\epsilon_k}\right] \ . \tag{5}$$

In the Minkowski-Bouligand method, $U(\epsilon)=E(\epsilon)$ is the union of all the disks centered on E with radius ϵ. In fact, Eq. (5) is general. The boxes or disks can be replaced with any geometric figure which has a diameter on the order of ϵ. If we denote these generic figures by A then the union of those A will constitute a generalized cover for E. Let $\mathcal{A}$ be the collection of those figures. It can be seen from previous examples that $\mathcal{A}$ can be finite, countable, or can have the power of the continuum. The only requirement for the figures A is that the closure $\overline{A}$ of A be homeomorphic to the disk.

To formalize the notion of a generalized cover; recall that the *diameter* of a figure A, denoted $\operatorname{diam}A$, is the largest distance between any two points of A. The *internal diameter* of A, denoted $\operatorname{diam}_{\text{int}}A$, is the diameter of the largest disk included in A.

We can now define a cover. Given two positive real numbers ϵ and $c, c\geq 1$, the (ϵ,c) cover for E is any set $U(\epsilon)$ that can be written as follows:

$$U(\epsilon)=\bigcup_{A\in\mathcal{A}}A \ ,$$

where $\mathcal{A}$ is a family of figures such that the following are true.

(i) $E\subset U(\epsilon)$.

(ii) For all $A\in\mathcal{A}$. A contains at least one point of E.

(iii) For all $A\in\mathcal{A}$, $\epsilon/c\leq\operatorname{diam}_{\text{int}}A\leq\operatorname{diam}A\leq c\epsilon$.

For the Minkowski cover, the figures A are disks, and the mapping from $\mathcal{A}$ onto E is one to one with $c=2$. For box counting, A are squares, $\mathcal{A}$ is finite [$\mathcal{A}$ is composed of $\Omega(E,\epsilon_k)$ elements], and $c=2\sqrt{2}$. By a theorem proved in Tricot *et al.*,[11] the fractal dimension is the same in each of these cases. Or, more formally, let c be a fixed constant with $0<c\leq 1$ and a family $U(\epsilon)$ of (ϵ,c) covers for E. Then

$$\Delta(E)=\lim_{\epsilon\to 0}\left[2-\frac{\ln|U(\epsilon)|_2}{\ln\epsilon}\right] \ . \tag{6}$$

Theoretically, if there is no limit, we define $\Delta(E)$ as an upper limit.

III. STANDARD ALGORITHMS FOR ESTIMATING FRACTAL DIMENSION OF PROFILES

We now compare the standard algorithms for estimating fractal dimension that have been developed from the background definitions in Sec. II. The complexity for each of these algorithms will be estimated to compare them both for practical applications and, more generally, as a basis for considering their extension to higher dimensions. The notation is standard throughout. We begin by discretizing the curve $f(x)$ into $N+1$ equally spaced points $f(x_n)$, $n=0,1,\ldots,N$. Observe that this introduced certain sampling errors. Furthermore, many of the algorithms function within the space in which the curve is embedded, which introduces additional quantization errors. For example, displaying the curve in a window discretizes the embedding space into $R \times S$ pixels. Since this projects the curve into a discrete domain, the fractal curve will then be approximated by a set of points $(x_n, f(x_n))$ linked by straight lines. The resulting curve is, of course less irregular than the theoretical curve, so one might expect an estimated fractal dimension smaller than the theoretical value.

Prototypical test curves. In order to test the various algorithms in this section we will use three different types of curves. The first test function that will be used is the trace of fractional Brownian motion[16] (FBM). It has been generated by the fast Fourier filtering technique described in Voss.[17] For this paper, we chose a FBM curve with dimension $\Delta(G_f)=1.4$ [Fig. 4(a)].

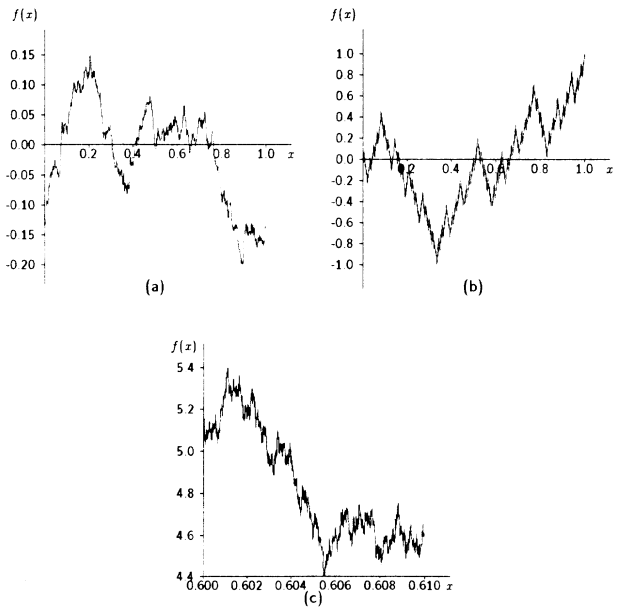

FIG. 4. Test objects with known fractal dimension. (a) Fractional Brownian motion (FBM) curve with $H=0.6$ leading to $\Delta(G_f)=1.4$; (b) Kiesswetter curve with fractal dimension $\Delta(G_f)=1.5$; and (c) Weierstrass-Mandelbrot (WM) curve with $b=2.1$ and $H=0.4$ leading to $\Delta(G_f)=1.6$. Note that in all the algorithms, the curves are mapped to the unit square.

The second test function belongs to a certain class of functions described in Dubuc and Elqortobi.[18] Those functions are bounded and defined on [0,1] with

$$f(0)=f_0=0,\quad f(1/p)=f_1,\quad f(2/p)=f_2\ ,$$
$$f(1)=f_p=1\ ,$$

where the number p is called the degree of the function. Any function f belonging to this class further has the property that on each interval $(i/p,(i+1)/p)$ (with $i=0,1,\ldots,p-1$), it reproduces what it is on (0,1), i.e.,

$$f(x)=f_i+(f_{i+1}-f_i)f(px-i)\ .$$

The function we chose has degree $p=4$ and is defined by

$$f_0=0,\quad f_1=-0.5,\quad f_2=0,\quad f_3=0.5,\quad f_4=1\ .$$

It is commonly referred to as the Kiesswetter curve[19] and has dimension $\Delta(G_f)=1.5$ [see Fig. 4(b)].

The last object, a mathematical model, is the Weierstrass-Mandelbrot function:

$$f(x)=\sum_{n=-\infty}^{\infty} b^{-nH}(1-\cos b^n x)\ ,$$

where $b>1$ and $0<H<1$. It is well established that $\Delta(E)=2-H$ (see Berry and Lewis[20]).

We chose this function since it has already been used to model rough surfaces.[21] The particular parameters chosen for our Weierstrass-Mandelbrot test curve are $b=2.1$, $H=0.4$ [then $\Delta(G_f)=1.6$] and with $0.60 \le x \le 0.61$. The resulting curve is shown in Fig. 4(c).

To facilitate comparison between the different algorithms, in all cases we chose $N=16\,384$ points.

Local fractal dimension. A feature that often helps to determine the range over which to compute the fractal dimension is the local fractal dimension,[8] or what might be thought of as a "sliding window" estimate (through ϵ) of the fractal dimension. To illustrate, one could compute the fractal dimension for the first 10 values of ϵ, then for 2 to 11, then 3 to 12, and so forth. If the log-log plot yields a straight line, the plot of the lower bound against the local fractal dimension will be constant and its value is reliably $\Delta(G_f)$. More generally, however, there may be only a limited range of values of ϵ where the log-log plot can yield accurate estimates of the fractal dimension.

A. Minkowski-Bouligand method

In order to get the Minkowski cover $G_f(\epsilon)$ we will use a basic concept from mathematical morphology[9] called *dilation*. Let B be a set that we will call a *structuring element*, and let B be swept over the embedding space (here a unit square in $\mathbb{R}^2$). If we note by B_x the structuring element B associated with position x, then the dilation of G_f by B is

$$Y=\{x:\ B_x \cap G_f \neq \emptyset\}\ . \tag{7}$$

The Minkowski cover in $\mathbb{R}^2$, as defined in Sec. II A, is equivalent to a dilation applied on G_f, the structuring element B being a disk with radius ϵ. Since we want

$G_f(\epsilon)$ for a range of ϵ ($\epsilon=1,2,\ldots,70$ pixels, for instance), we would have to apply the dilation over and over again. But *distance transforms* can accomplish the same result more efficiently. In particular, a distance transform takes a binary image $b(i,j)$, where

$$b(i,j)=\begin{cases}1 & \text{if } (i,j) \text{ is an object point}\\ 0 & \text{if } (i,j) \text{ is a background point}\end{cases}$$

and converts it into a minimal distance array $d(i,j)$ in which each element has a value equal to its minimal distance to the object, given a particular metric. Figure 5 shows the minimal distance array for the Kiesswetter curve. The algorithm that we shall use is called the "chamfer 5-7-11" distance transform.[22] It is a recursive algorithm and it provides a very good approximation to the Euclidean distance. Finally, the histogram of the minimal distance array can then be used to compute the $|G_f(\epsilon)|_2$ needed for the log-log plot.

The algorithm to get the log-log data with the Minkowski-Bouligand method [Eq. (2)] can be divided into four steps. We assume that we have a list of $N+1$ points $(x_n, f(x_n))$ and an $R\times S$ array.

(1) Position the points $f(x_n)$ into the binary array linking them by straight lines.

(2) Compute the distance transform from the binary array and get the minimal distance array.

(3) Compute the histogram of the minimal distance array.

(4) From the histogram, get the $|G_f(\epsilon)|_2$.

The complexity of the Minkowski-Bouligand algorithm can be estimated as follows. The first step is $O(N)$. The second and third steps are $O(RS)$. The length of the histogram array being fixed, the last step is $O(1)$. The result is then an algorithm which is $O(RS)$.

1. Results on test curves for the Minkowski-Bouligand method

We applied the algorithm to the prototypical test curves presented at the beginning of Sec. III. The results are shown in Table I. Observe that the error, i.e., the deviation of the estimated dimension from the theoretical one, is significant. The log-log plots and local fractal dimension graphs are presented in Fig. 6. If the local fractal dimension estimates are consistent everywhere, then they would yield the solid horizontal line shown. However, in all cases note that the local fractal dimension [Figs. 6(b), 6(d), and 6(f)] is nowhere constant, preventing a con-

FIG. 5. Distance transform applied to the Kiesswetter curve of Fig. 4(b). The distance is displayed as a gray level intensity: dark corresponds to points close to the object and bright to points that are far away.

TABLE I. Estimation errors when applying the Minkowski-Bouligand method. The first column gives the theoretical fractal dimension, the second column shows the estimated fractal dimension, and the third column gives the deviation from the true value.

Object	$\Delta(G_f)$	$\Delta_e(G_f)$	Deviation
FBM curve	1.4	1.313	0.087
K curve	1.5	1.356	0.144
WM curve	1.6	1.380	0.220

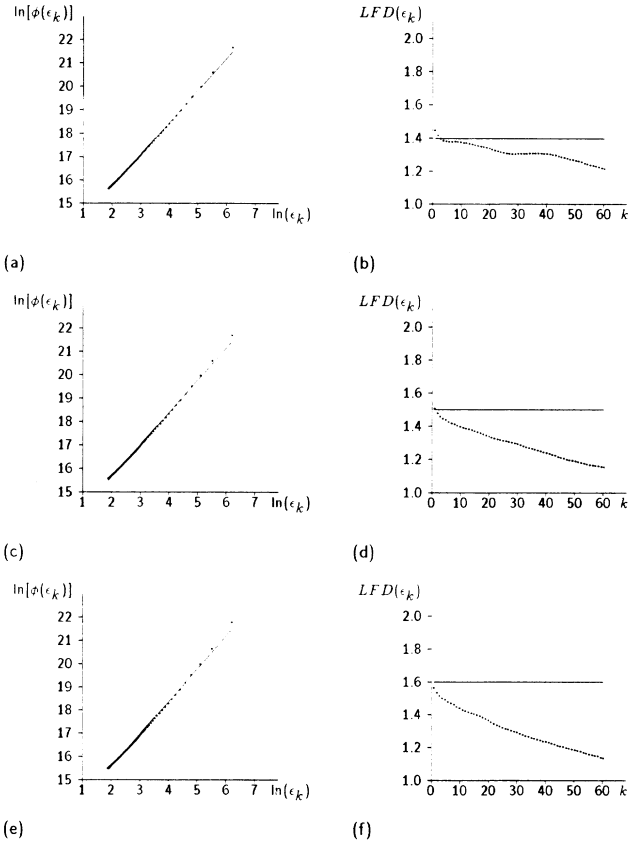

FIG. 6. Evaluation of the fractal dimension of the test curves using the Minkowski-Bouligand method. (a) and (b) are for the FBM curve, (c) and (d) for the Kiesswetter curve, and (e) and (f) for the WM curve. The left column presents the log-log plots with $\phi(\epsilon_k)=|G_f(\epsilon_k)|_2$, while on the right we present the graphs of the local fractal dimension. In the ideal case, the log-log plots (on the left) would lie on perfectly straight lines, and the local fractal dimension (right) could be horizontal solid straight lines. However, observe the concavity in plots (a), (c), and (e), significantly confusing the straight-line fit and the skewing of the local fractal dimension (LFD) estimates away from the horizontal straight line.

sistent estimate of $\Delta(G_f)$. For those in that example we had $R=S=400$ and the range chosen was $\epsilon_k=k/R$ where $k=1,2,\ldots,70$.

2. *Discussion of the Minkowski-Bouligand method*

The precision of the Minkowski-Bouligand method is poor since the points defined in Eq. (2) almost never lie on a straight line. Consider a simple example: if G_f is a segment with length l, then $|G_f(\epsilon)|_2=2l\epsilon+\pi\epsilon^2$. Since this area is not directly proportional to ϵ, the log-log plot results in a concave curve instead of a straight line, and a close examination of Figs. 6(a), 6(c), and 6(e) reveals the concavity. This problem is even worse when the curve has an infinite number of local minima. The basic problem, in some sense, is that the Minkowski cover is too "thick." The presence of the "rolls" in the sausage (Fig. 7) induces a concavity in the log-log plot which does not allow a precise estimate of the fractal dimension. Those rolls are even more dominant when ϵ_k is large and R and S are small.

B. Box-counting method

This method is straightforward to implement. Once the object is "drawn" in the binary array, the definition can be applied directly with $\epsilon_k=k/R$, $k=2,3,\ldots,k_{\max}$, where $k_{\max}\ll R$. Assuming that $k_{\max}$ is a constant, this algorithm is $O(RS)$.

1. *Results on test curves for the box-counting method*

We have in Fig. 8(c) the log-log plot for the Kiesswetter curve with $R=S=400$ and $k_{\max}=70$. Notice the jumps and the dispersion of the points for large ϵ_k. The same sort of behavior can be observed for the Weierstrass-Mandelbrot (WM) and the FBM curves in Figs. 8(a) and 8(e). This then results in instabilities in the local fractal dimension plot as one can see in Figs. 8(b), 8(d), and 8(f). However, for small ϵ the local fractal dimension is "not bad" especially in the case of the Kiesswetter curve and the FBM curve. But to date no algorithm is known for optimally selecting points to improve the dimension estimate. The results for the estimation of the fractal dimension $\Delta_e(G_f)$ using this method are presented in Table II.

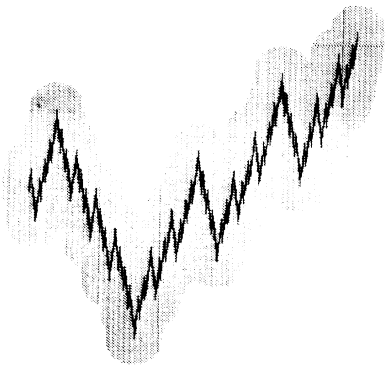

FIG. 7. Minkowski cover for the Kiesswetter curve. Notice the "rolls" that occur at the location of the local minima and local maxima.

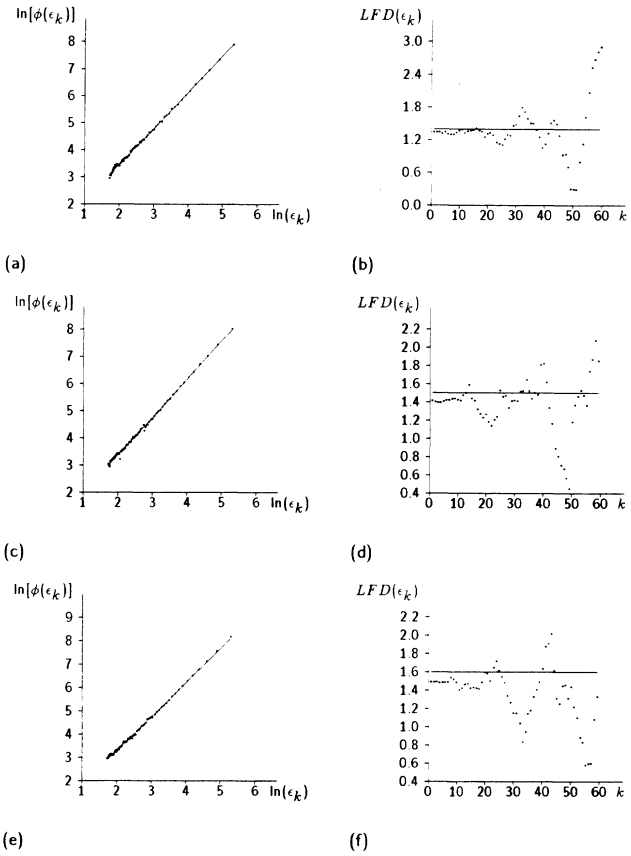

FIG. 8. Evaluation of the fractal dimension of the test curves using the box-counting method: (a) and (b) for the FBM curve, (c) and (d) for the Kiesswetter curve, and (e) and (f) for the WM curve. The left column presents the log-log plots with $\phi(\epsilon_k)=\Omega(G_f,\epsilon_k)$, while on the right we have the graphs of the local fractal dimension. Observe the scatter in the local fractal dimension (LFD) graphs; such scatter is inherent in the box-counting method.

2. *Discussion of the box-counting method*

Although very simple to use, the box-counting method has many drawbacks. First, the characteristic jumps prevent a continuous log-log plot; the scatter is every-

TABLE II. Estimation errors for the box-counting method. The first column gives the theoretical fractal dimension. The middle two columns present the results using all the points present in the log-log plots of Fig. 8, while the last two columns present the results when fitting the line through the first 20 points only.

Object	$\Delta(G_f)$	$\Delta_e(G_f)$	Deviation	$\Delta_e(G_f)$	Deviation
FBM curve	1.4	1.335	0.065	1.338	0.062
K curve	1.5	1.392	0.108	1.413	0.087
WM curve	1.6	1.443	0.157	1.491	0.109

where. It is almost impossible to eliminate this scatter, since $\Omega(G_f,\epsilon_k)$ can only take integer values, thereby inducing big jumps in the transition from ϵ_k to ϵ_{k+1}. Another problem is that if $1/\epsilon_k$ is not an integer, then the pixels with side ϵ_k will "overflow" on both sides of the graph G_f. This will bias the results and introduce irregularities in the log-log plot [Eq. (4)], especially when ϵ_k is large. One would like all the boxes to fit exactly into the unit square. this is possible for all ϵ_k if $\epsilon_k=2^k/R$ with $R=2^l$, i.e., if ϵ_k and R are dyadic numbers. However, if this sequence, which tends to zero quite fast, were used, the precision of the data would rapidly be reached and the computation would have to stop: the log-log plot [Eq. (4)] would then contain only a very few points and accurate fits would be elusive. Although methods have been introduced to correct the errors due to a sequence ϵ_k of nondyadic numbers,[13] the errors due to the discontinuities are not correctable without altering the algorithm substantially. Furthermore, this method is very sensitive to quantization. Small values of R and S are equivalent to large values of ϵ_k, leading to severe discontinuities in the log-log plot and yielding less accurate results.

C. Power spectrum method

The power spectrum method is widely used for applications in materials science. Descriptions of this method can be found in Voss,[23] Pfeifer,[1] and Pentland.[7] In the case of self-affine functions, a relationship exists between the power spectrum and the fractal dimension,[24] so that the fractal dimension of a self-affine curve can be obtained from the log-log plot:

$$(\ln\omega,\ \ln[\omega^5 P_f(\omega)]^{1/2}) , \tag{8}$$

where $P_f(\omega)$ is the power spectrum of f.

Given the profile data, a 1D fast Fourier transform (FFT) can be used to compute the power spectrum. The slope of the line passing through the points of Eq. (8) should provide the fractal dimension. Since it is known that the FFT is $O(N\ln N)$ in terms of complexity, it would result in an algorithm which is $O(N\ln N)$. The precision of the method, however, is relatively low, as we show in Sec. III C 1.

1. *Example and discussion*

One problem with the power spectrum method is that the points in the log-log plot rarely lie on a straight line, which makes the evaluation of $\Delta(G_f)$ difficult. The method has been applied to our test curves and typical log-log plots are shown in Fig. 9. Even if we apply local average correction the fit is good only for particular cases. The results of the estimation of the fractal dimension using this method are presented in Table III.

The difficulties with the power spectrum method go beyond a consideration of accuracy alone. In order to use this method, one has to make the hypothesis that the set under study is self-affine, which is quite restrictive.[24] However, even if this hypothesis were true, the fact that there are only a finite number of points makes it difficult to obtain a good fit. Moreover, based on analysis by Dekking and Van Otterloo,[25] we conjecture that the power spectrum does not have a specific rate of convergence, but rather decreases at least as fast as $O(\omega^{-\alpha})$. This raises further complications in estimating fractal dimension from it.

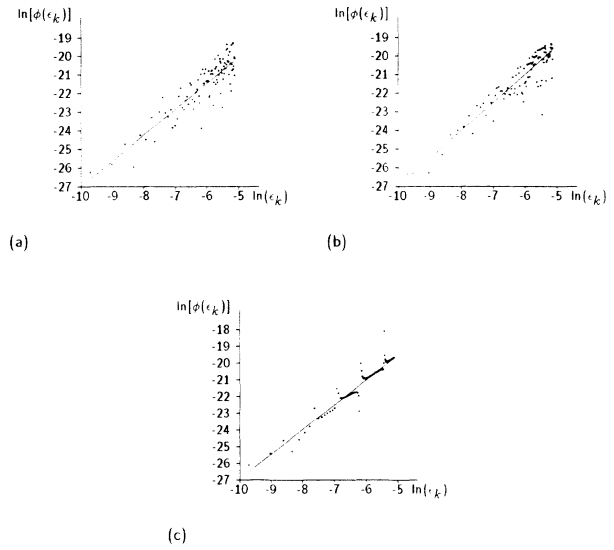

FIG. 9. Evaluation of the fractal dimension of the test curves using the power spectrum method: log-log plots for (a) the FBM curve, (b) the Kiesswetter curve, and (c) the WM curve. For all those plots $\phi(\epsilon_k)=P_f(\epsilon_k)$. Observe the point dispersion which distorts the straight-line fit.

IV. NEW ALGORITHMS FOR ESTIMATING THE FRACTAL DIMENSION OF PROFILES

As we have shown, the standard algorithms are neither robust nor efficient. In this section, which is the heart of the paper, we introduce two new algorithms for computing the fractal dimension. The first of them—called the *horizontal structuring element method* (HSEM)—derives from the Minkowski cover discussed previously, but leads to more accurate results by eliminating the "folds" in the sausage. But the HSEM is just an intermediate step. It introduces the idea of building covers out of intervals rather than figures, an idea that is more fully exploited in our second algorithm: the *variation method.* It is the variation method that yields the most robust and efficient estimates of fractal dimension.

TABLE III. Estimation errors when applying the power spectrum method. In the first column we have the theoretical fractal dimension, the second column presents the estimated value, and the third column shows the deviation from the true value.

Object	$\Delta(G_f)$	$\Delta_e(G_f)$	Deviation
FBM curve	1.4	1.418	0.018
K curve	1.5	1.449	0.051
WM curve	1.6	1.526	0.074

A. Horizontal structuring element method

For the Minkowski cover, the "rolls" induce a concavity in the log-log plot, confusing the line fit. Most concavities appear at the peaks (local maxima and minima) of the function. For self-affine and related graphs, it is better to use structuring elements which are invariant under affine transformations. Instead of disks then, we will use horizontal segments, thus cutting off portions of disks at the peaks of the graph.

To be more precise, for all x in [0,1], let us call $T(x,\epsilon)=[x-\epsilon, x+\epsilon]\times\{f(x)\}$ the horizontal segment of length 2ϵ, center at $(x, f(x))$ on G_f. Let

$$U(\epsilon)=\bigcup_{0\le x\le 1} T(x,\epsilon) \tag{9}$$

be the union of all those structuring elements. Since f is continuous we see that $U(\epsilon)$ has a nonzero area, except in the special case where f is constant, and this can be used to calculate the fractal dimension. In particular, if $U(\epsilon)$ is as defined in Eq. (9), we have

$$\Delta(G_f)=\max\left[1, \lim_{\epsilon\to 0}\left[2-\frac{\ln|U(\epsilon)|_2}{\ln\epsilon}\right]\right] . \tag{10}$$

Because of the importance of the "horizontal segment" covers in the HSEM, we now present a proof of assertion (10). Let

$$\Delta^*=\lim_{\epsilon\to 0}\left[2-\frac{\ln|U(\epsilon)|_2}{\ln\epsilon}\right] .$$

For all x, $0\le x\le 1$, let $C(x,\epsilon)$ be the square

$$[x-\epsilon, x+\epsilon]\times[f(x)-\epsilon, f(x)+\epsilon] .$$

Finally, let

$$V(\epsilon)=\bigcup_{0\le x\le 1} C(x,\epsilon)$$

be the union of all those squares: it is an $(\epsilon, 2\sqrt{2})$ cover as described in Sec. II and it satisfies Eq. (10). We always have $\Delta(G_f)\ge 1$. Since $U(\epsilon)$ is included in $V(\epsilon)$, we get $\Delta^*\le\Delta(G_f)$, leading to

$$\Delta(G_f)\ge\max(1,\Delta^*) .$$

To probe Eq. (10), we now show that the inequality holds in the other direction as well. Let $H(\epsilon)$ be the set of all x such that for all $x'\in[x-\epsilon,x+\epsilon]$, we have $|f(x')-f(x)|\le\epsilon$. Let

$$V_1=\bigcup_{x\notin H(\epsilon)} C(x,\epsilon), \quad V_2=\bigcup_{x\in H(\epsilon)} C(x,\epsilon) .$$

We now estimate the area of those two sets.

(a) If $x\notin H(\epsilon)$, then there exists an x' such that $|x-x'|\le\epsilon$, and $|f(x)-f(x')|=\epsilon$. If $C(x,\epsilon)$ is divided into four squares with side ϵ, then at least one of those squares is included in $U(\epsilon)$. If we call D_x the inscribed disk in this subsquare, and D_x' the disk with the same center but radius $2\sqrt{2}\epsilon$ [which contains $C(x,\epsilon)$], we have

$$|\cup D_x'|_2\le c|\cup D_x|_2 , \tag{11}$$

where c is a real number independent of ϵ. This follows from the following observation. Let $0<a<b$, and let a family of disks D with diameter a be given. Now, if for all D, we let D' be a disk with the same center and with diameter b, then

$$a^2|\cup D'|_2\le b^2|\cup D|_2 .$$

Specifically, for inequality (11) this implies

$$|V_1|_2\le c|U(\epsilon)|_2 . \tag{12}$$

(b) Define a *section* of $V_2(x)$ to be the (linear) set of points of V_2 with abscissa x. Now choose x such that the section of V_2 with respect to x is nonempty, and call $l(x)$ the measure (length) of this section. We have $l(x)\ge 2\epsilon$. On the other hand, we can show that

$$l(x)\le 6\epsilon . \tag{13}$$

Indeed, if $l(x)>6\epsilon$, then the section of V_2 with respect to x contains the section of at least three disjoint squares of the type $C(x',\epsilon)$, with $x'\in H(\epsilon)$. In other words, at least three points of $H(\epsilon)$ exist, say, x_1,x_2,x_3, with a distance to x less than ϵ. Among those three points, at least two, for example, x_1 and x_2, are on the same side of x: consequently, $|x_1-x_2|\le\epsilon$ and $|f(x_1)-f(x_2)|\ge 2\epsilon$ since their respective squares are disjoint. But this is a contradiction with the fact that those points are in $H(\epsilon)$. This inequality (13) being true, Fubini's theorem[26] states that the area of a set is equal to the integral of the lengths of its sections, therefore

$$|V_2|_2\le 6\epsilon . \tag{14}$$

(c) Conclusion: (12) and (14) give

$$|V(\epsilon)|_2\le 6\epsilon+c|U(\epsilon)|_2 .$$

For all α, $0\le\alpha\le 2$, we get

$$\epsilon^{\alpha-2}|V(\epsilon)|_2\le 6\epsilon^{\alpha-1}+c\epsilon^{\alpha-2}|U(\epsilon)|_2 .$$

The critical values of α, for the three terms of this inequality, are, respectively, $\Delta(G_f)$, 1, and Δ^*. Finally, then, it follows that

$$\Delta(G_f)\le\max(1,\Delta^*) ,$$

which completes the proof.

For calculations, it is better to consider the points of $U(\epsilon)$ for which the x coordinate lies between 0 and 1. In other words, if we let

$$T'(x,\epsilon)=[\max(0,x-\epsilon), \min(1,x+\epsilon)]\times\{f(x)\}$$

be the part of $T(x,\epsilon)$ which projects onto [0,1], we can replace $U(\epsilon)$ with

$$U'(\epsilon)=\bigcup_{0\le x\le 1} T'(x,\epsilon) . \tag{15}$$

It is clear that this change hardly affects the calculations described earlier, and (10) is still valid with $U'(\epsilon)$.

Finally, observe that the profiles that we want to study are clearly not rectifiable: we can therefore assume that their fractal dimension is greater than 1. Hence it is not

necessary to keep the maximum in Eq. (10), and for calculations, the corresponding log-log plot is

$$(\ln(1/\epsilon), \ln[(1/\epsilon^2)|U'(\epsilon)|_2]) \ . \tag{16}$$

1. Implementation

The implementation of the horizontal structuring element is quite similar to the Minkowski-Bouligand implementation presented in Sec. III A. Since information for a range of ϵ is needed, the distance transforms can again be used. The "multidilation" with a segment as structuring element is equivalent to performing a unidimensional distance transform[22] on each line of the binary array $b(i,j)$. The result is a minimal distance array $d(i,j)$ into which each pixel has a value equal to its minimal distance to $E \cap j$ (Fig. 10), i.e.,

$$d(i,j) = \min_{(s,t)\in E\cap j} |s-i| \ .$$

Once the minimal distance array is obtained, the rest of the algorithm is absolutely the same as the Minkowski-cover case.

The undimensional distance transform part will still be $O(RS)$, but the constant is smaller than in the "chamfer 5-7-11" distance transform. The algorithm is therefore still $O(RS)$.

2. HSEM: results on test curves and discussion

The algorithm has been run on the usual test curves. Figs 11(b), 11(d), and 11(f) give the local fractal dimension. The log-log plots look much better than for the Minkowski-Bouligand or the box-counting method, although the results are still not perfect. The estimates $\Delta_e(G_f)$ are shown in Table IV.

With the horizontal structuring element method, we succeeded in eliminating the rolls that were present in the Minkowski-Bouligand method. However, the method is still dependent on the size of the window, with smaller R and S leading to large quantization errors. Also, efficiency is still a problem, having not reduced the complexity from $O(RS)$. For generalization to higher dimensions one would prefer an algorithm that is $O(N)$, where N is the number of points that approximate the curve. This leads us to the variation method.

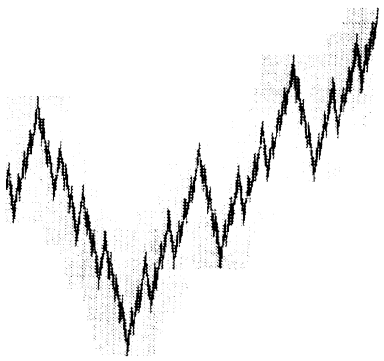

FIG. 10. "Horizontal structuring element" cover for the Kiesswetter curve. This figure presents the result of dilating the object G_f with a horizontal segment as structuring element. The cover $U'(\epsilon)$ as defined in Eq. (15) is displayed in gray. Notice that the rolls that were present in the Minkowski cover (Fig. 7) and box-counting figures are now eliminated.

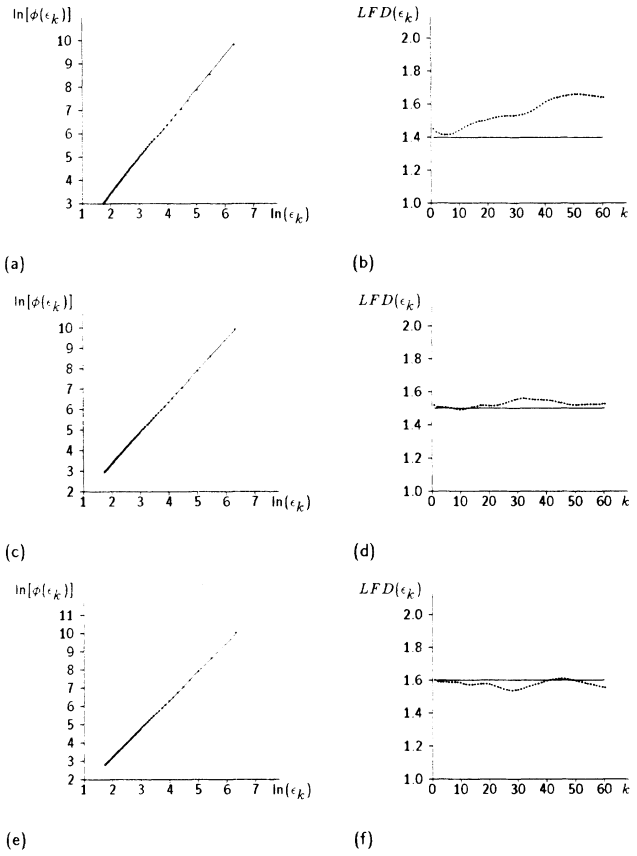

FIG. 11. Estimation of the fractal dimension with the horizontal structuring elements method. (a) and (b) are for the FBM curve, (c) and (d) for the Kiesswetter curve, and (e) and (f) for the WM curve. The left column presents the log-log plots with $\phi(\epsilon_k) = |U'(\epsilon_k)|_2$, while on the right we present the graphs of the local fractal dimension.

B. Variation method

We begin with a different presentation of the HSEM. If the graph G_f of f is fractal, there exists at least one part of the interval [0,1] on which f is nowhere or almost nowhere differentiable. If $p(x,x')$ is the slope of the line

TABLE IV. Estimation errors when applying the HSEM. First column, theoretical fractal dimension; second column, estimated fractal dimension; third column, deviation from the true value.

Object	$\Delta(G_f)$	$\Delta_e(G_f)$	Deviation
FBM curve	1.4	1.482	0.082
K curve	1.5	1.537	0.037
WM curve	1.6	1.595	0.005

passing through $(x, f(x))$ and $(x', f(x'))$ of the graph, the fractal concept is related to the following property: the upper limit of the absolute value $|p(x,x')|$ is infinite when x' tends toward x. It is the rate of growth of this convergence that determines the fractal dimension. It depends on the Hölder local properties of f (see Tricot[27]), themselves related to the fractional derivatives of f. In order to measure this behavior, we define a function of two variables related to f.

Formally, the ϵ oscillation $v(x,\epsilon)$ of the function f in x is given by

$$v(x,\epsilon)=\sup_{x'\in R_\epsilon(x)} f(x')-\inf_{x'\in R_\epsilon(x)} f(x') , \tag{17}$$

where $R_\epsilon(x)=\{s:\ |x-s|<\epsilon \text{ and } s\in[0,1]\}$, and the ϵ variation $V(\epsilon,f)$ of the function f is given by

$$V(\epsilon,f)=\int_0^1 v(x,\epsilon)dx .$$

Since f is continuous, the ϵ variation of f tends to 0 as ϵ tends toward 0. It is the rate of growth of the ϵ variation that is directly related to the dimension of G_f. In fact, we shall show that if $U'(\epsilon)$ is the cover defined in Eq. (15) with the union of horizontal structuring elements, restricted to the abscissa included between 0 and 1, then

$$|U'(\epsilon)|_2=V(\epsilon,f)=\int_0^1 v(x,\epsilon)dx . \tag{18}$$

The proof proceeds as follows. For all x, let us call $S(x,\epsilon)$ the vertical segment whose external coordinates are

$$(x,\ \sup_{|x-x'|\le\epsilon} f(x'))$$

and

$$(x,\ \inf_{|x-x'|\le\epsilon} f(x')) ,$$

respectively. Its length is $v(x,\epsilon)$. Let

$$W(\epsilon)=\bigcup_{0\le x\le 1} S(x,\epsilon) \tag{19}$$

be the union of all those segments. Using Fubini's theorem, which says that the area is equal to the integral of the sections, if we take the vertical sections of $W(\epsilon)$ to be the segments $S(x,\epsilon)$, then we have

$$|W(\epsilon)|_2=\int_0^1 v(x,\epsilon)dx .$$

It remains to prove that the sets $U'(\epsilon)$ and $W(\epsilon)$ are identical. Let (x,y) be a point in $W(\epsilon)$. The ordinate y lies between the upper bound and the lower bound of

$$\{f(x'):\ |x-x'|\le\epsilon\} .$$

Since f is continuous, there exists an x_0, $|x_0-x|\le\epsilon$, such that $f(x_0)=y$. Then (x,y) belongs to the horizontal segment $T'(x_0,\epsilon)$. Hence

$$W(\epsilon)\subset U'(\epsilon) .$$

For the other side, let (x,y) be a point in $U'(\epsilon)$. There exists an x_1 such that $(x,y)\in T'(x_1,\epsilon)$, i.e., $y=f(x_1)$ and $|x-x_1|\le\epsilon$. Since (x_1,y) is a point of the graph, then y lies between the upper and the lower bound of

$$\{f(x'):\ |x-x'|\le\epsilon\} .$$

Thus (x,y) belongs to the vertical segment $S(x,\epsilon)$, and

$$U'(\epsilon)\subset W(\epsilon) .$$

To estimate fractal dimension using the variation idea, observe that Eq. (10) can be replaced by

$$\Delta(G_f)=\max\left[1,\ \lim_{\epsilon\to 0}\left[2-\frac{\ln\left(\int_0^1 v(x,\epsilon)dx\right)}{\ln\epsilon}\right]\right] . \tag{20}$$

The corresponding log-log plot for the calculation is then

$$\left[\ln(1/\epsilon),\ \ln\left[\frac{1}{\epsilon^2}\int_0^1 v(x,\epsilon)dx\right]\right] . \tag{21}$$

The first attempt to use such a method for a real problem in materials science is in Quiniou.[28]

1. Implementation

Based on the definition of the variation dimension, it is straightforward to develop an algorithm for estimating the fractal dimension of 1D profiles. It is important, however, to have an efficient implementation of the algorithm or the computation could be very expensive, especially for generalizations to higher dimensions. In this section we present such an implementation and in Sec. IV B 2 we show that the resulting method yields accurate results on curves with known fractal dimension.

Suppose that the digitized profile data are $f(n/N)$, $n=0,1,\ldots,N$. Given a list of integers in increasing order k_i, $i=1,2,\ldots,i_{\max}$, we would like to compute the log-log data of Eq. (21). In particular, this involves computing

$$V(\epsilon_i,f)=\int_0^1 v(x,k_i/N)dx \quad \text{where } \epsilon_i=\frac{k_i}{N}$$

for $i=1,2,\ldots,i_{\max}$. Let us define two new functions, u and b, that we call the upper envelope and the lower (bottom) envelope (after Peleg *et al.*,[8]), respectively (see Fig. 12). Formally, the upper ϵ envelope $u_\epsilon(x)$ and lower ϵ envelope $b_\epsilon(x)$ are defined as follows:

$$u_\epsilon(x)=\sup_{x'\in R_\epsilon(x)} f(x') ,$$

$$b_\epsilon(x)=\inf_{x'\in R_\epsilon(x)} f(x') ,$$

where $R_\epsilon(x)=\{s:\ |x-s|\le\epsilon \text{ and } s\in[0,1]\}$. It follows immediately that

$$V_\epsilon(f)=\int_0^1 [u_\epsilon(x)-b_\epsilon(x)]dx .$$

Since the curve is digitized, we make the following approximation:

$$\hat{u}_i(n)=\max_{n-k_i\le j\le n+k_i} f(j/N) ,$$

$$\hat{b}_i(n)=\min_{n-k_i\le j\le n+k_i} f(j/N) , \tag{22}$$

with $0 \le n \le N$ and where $\hat{u}_i(n)$ $[\hat{b}_i(n)]$ is the approximation to $u_{\epsilon_i}(n/N)$ $[b_{\epsilon_i}(n/N)]$. (One has to be careful at the borders. In Eq. (22), we compute the minimum and the maximum for $j/N \in [0,1]$.) However, if the k_i are relatively close to one another (i.e., if $\delta_i = k_i - k_{i-1} \le k_{i-1}$), then $\hat{u}_{i-1}$ and $\hat{b}_{i-1}$ can be used to compute $\hat{u}_i$ and $\hat{b}_i$ (see Dubuc[29]):

$$\begin{aligned} \hat{u}_i(n) &= \max(\hat{u}_{i-1}(n-\delta_i), \hat{u}_{i-1}(n+\delta_i)) , \\ \hat{b}_i(n) &= \min(\hat{b}_{i-1}(n-\delta_i), \hat{b}_{i-1}(n+\delta_i)) . \end{aligned} \tag{23}$$

In other words, a pyramid can be constructed in which the information at a previous level can be used to compute the information at the current level, reducing the complexity of the algorithm. We finally make the following approximation:

$$\int_0^1 v(x,k_i/N)dx \approx \frac{1}{N+1} \sum_{n=0}^{N} \hat{u}_i(n) - \hat{b}_i(n).$$

However, this might not give the best estimates of the variation when ϵ_i is small, for the following reason: if the curve is digitized into $N+1$ points, then the smallest ϵ_i possible is $\epsilon_i = 1/N$. For that value of ϵ_i, according to Eq. (22), we would have

$$u_{1/N}(n/N) \approx \hat{u}_1(n) = \max(f((n-1)/N), f(n/N), f((n+1)/N)) ,$$
$$b_{1/N}(n/N) \approx \hat{b}_1(n) = \min(f((n-1)/N), f(n/N), f((n+1)/N)) ,$$

i.e., the maximum and the minimum of the function in a $1/N$-neighborhood are evaluated over three points. This approximation should be reasonable if the fractal dimension of the curve is low (less than 1.5) but can be very poor if the fractal dimension of the curve is large (above 1.5). More points are needed to accurately estimate the maximum and the minimum in a $1/N$ neighborhood. We therefore reorganize the data so that estimates are made not at the $N+1$ distinct points, but rather at $R+1 \le N$ equidistant points. Then we would have $\epsilon_i = k_i/R$ and the envelopes for the smallest ϵ_i would be approximated as follows:

$$u_{1/R}(r/R) \approx \hat{u}_1(r) = \max_{(r-1)/R \le n/N \le (r+1)/R} f(n/N) ,$$
$$b_{1/R}(r/R) \approx \hat{b}_1(r) = \min_{(r-1)/R \le n/N \le (r+1)/R} f(n/N) .$$

R is chosen so that (i) it is small enough to give reliable estimates of the maximum and the minimum in each $1/R$ neighborhood, but (ii) large enough so that $V(\epsilon_i, f)$, for $\epsilon_i = k_i/R$, suitably approximates the limit as ϵ tends to 0. We will denote by R_{opt} the "best" R that can be chosen, in the sense that the reorganization of the points then minimizes the error in the fit of the log-log plot. R_{opt} can be found by scanning over the range of all possible R (i.e., applying the variation method for all possible values of R between 1 and N) and choosing the one that minimizes the fit. We have to note that, using this approach, the digital implementation of the variation method gives results that differ from those obtained with the HSEM. This is due to the fact that R varies from one curve to another (and is chosen to be optimal) rather than taking a fixed value (i.e., $R = 400$, in our case, for the HSEM). We thus expect more reliable results from the variation method. For the rest of this section we suppose that R is set to R_{opt}.

Given R, the ϵ variation is approximated as follows:

$$\int_0^1 v(x,\epsilon_i)dx \approx \frac{1}{R+1} \sum_{n=0}^{R-1} \hat{u}_i(n) - \hat{b}_i(n) \quad \text{with } \epsilon_i = \frac{k_i}{R} .$$

Since R does not depend on i, the corresponding log-log plot for evaluating $\Delta(G_f)$ is

$$\left[\ln\frac{1}{k_i}, \ln\left[\frac{1}{k_i^2} \sum_{n=0}^{R-1} \hat{u}_i(n) - \hat{b}_i(n) \right] \right], \quad i = 1,2,\ldots,i_{\max} .$$

A pseudocode version of the algorithm just described is given in Table V.

With the assumption that $k_i - k_{i-1} \le k_{i-1}$ (which is almost always the case) for each k_i, $i = 2,\ldots,i_{\max}$, the algorithm consists of $4R$ comparisons. Since we assume that $i_{\max}$ is a constant, the algorithm is $O(R)$. This is a substantial improvement over the standard techniques, in terms of both complexity and memory requirements.

2. *Results on test curves for the variation method*

When the variation algorithm is applied to the test curves, note that the estimated local fractal dimension (dotted line) [Figs. 13(b), 13(d), and 13(f)] is very close to the true value for the dimension (solid line). Notice also that in the log-log plots [Figs. 13(a), 13(c), and 13(e)] the points really lie on a straight line, as opposed to the Minkowski-Bouligand or the box-counting examples. The evaluation errors using this technique are shown in

TABLE V. Pseudocode for the 1D variation method to illustrate the key steps in the computation. In this pseudocode version, we omitted implementation details such as what to do on the borders, how to implement it with just one matrix, etc.

```
[1]   Compute û_1 and b̂_1;
[2]   For i = 2 to i_max do;
        δ = k_i − k_{i−1};
        For n = 0 to R do;
            û_i(n) = max[û_{i−1}(n − δ), û_{i−1}(n + δ)];
            b̂_i(n) = min[b̂_{i−1}(n − δ), b̂_{i−1}(n + δ)];
        end;
      end;
[3]   Compute log-log data
```

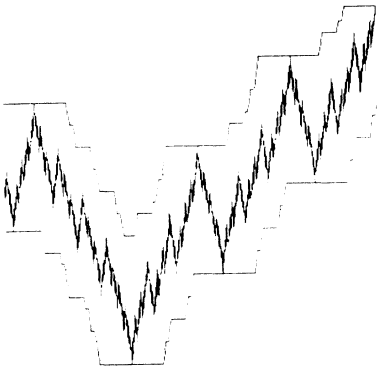

FIG. 12. "Variation cover" for the Kiesswetter curve. This figure shows the function f with the upper envelope u and the lower envelope b. Here we had $R=350$, $N=4096$. We plotted $\hat{u}_{30}(x)$ and $\hat{b}_{30}(x)$. Notice that the area bounded by $\hat{u}$ and $\hat{b}$ is equivalent to the gray area we had in Fig. 10.

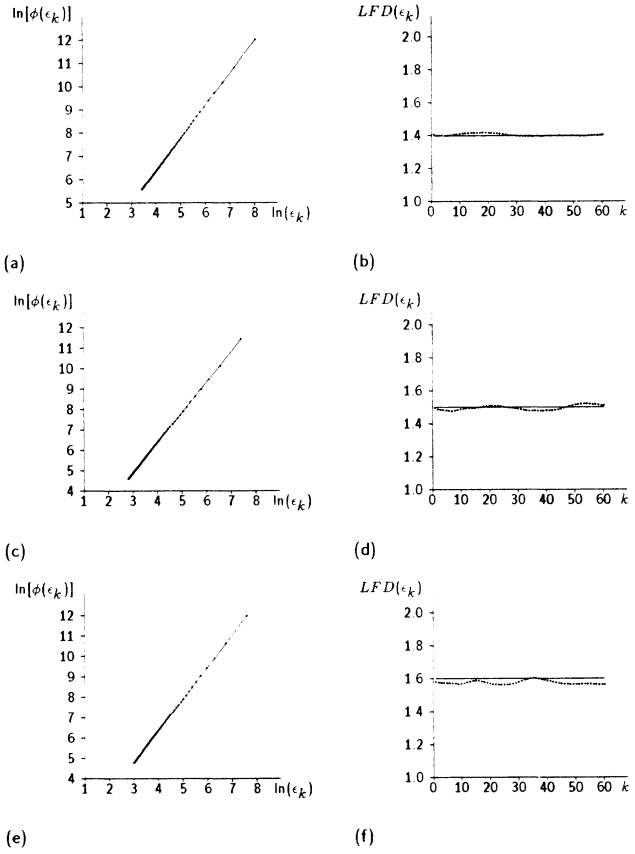

FIG. 13. Estimation of the fractal dimension with the variation method. (a) and (b) are for the FBM curve, (c) and (d) for the Kiesswetter curve, and (e) and (f) for the WM curve. The left column presents the log-log plots with $\phi(\epsilon_k)=V(\epsilon_k,f)$, while on the right we present the graphs of the local fractal dimension.

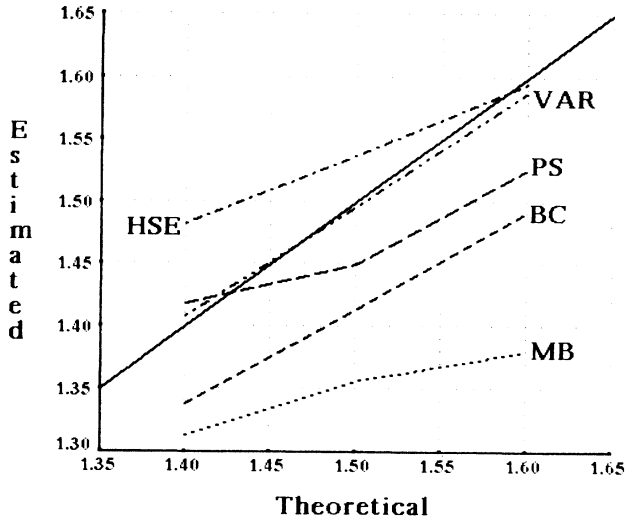

FIG. 14. Summary plot of estimated vs theoretical fractal dimension for all the test examples in the paper. Ideal behavior is indicated by the solid line, or which estimated fractal dimension equals theoretical fractal dimension. Distance from this solid line therefore indicates performance deficit. In this plot, MB stands for the Minkowski-Bouligand method, BC for the box-counting method, PS for the power spectrum method, HSE for the horizontal structuring elements method and VAR for the 1D variation method. This plot is a graphical recapitulation of what was presented in Tables I–IV and VI.

Table VI, and from that we see that it is significantly more accurate than the other "standard" algorithms. In this example $R=2200$ (for the Kiesswetter curve), $R=1000$ (for the WM curve), and $R=5120$ (for the FBM curve) were chosen.

C. Summary

To summarize all the experiments with objects of known fractal dimension, we plot in Fig. 14 the estimated fractal dimension versus the theoretical fractal dimension for each of the algorithms presented in Secs. III and IV. Ideal behavior is indicated by the solid line. Among the algorithms examined, for the Weierstrass-Mandelbrot, fractional Brownian motion, and Kiesswetter profiles, the variation method clearly performs the best.

V. CONCLUSIONS

The concept of fractal dimension is connected to the notion of roughness, a key variable in many physical situ-

TABLE VI. Estimation errors when applying the variation method. First column, theoretical fractal dimension; second column, estimated fractal dimension; third column, deviation from the true value.

Object	$\Delta(G_f)$	$\Delta_e(G_f)$	Deviation
FBM curve	1.4	1.408	0.008
K curve	1.5	1.495	0.005
WM curve	1.6	1.588	0.012

ations, so algorithms for measuring it are becoming widespread in both theory and applications. However, what appears to be the unexamined assumption behind the algorithms is that, since fractal dimension is well defined mathematically, then the algorithms derived from the definitions should work correctly as well. But this is not the case, as we showed in this paper by evaluating the fractal dimension of several well-known mathematical objects with the standard algorithms. The mathematical objects were chosen both because we could compute their fractal dimension exactly, and because they provide profiles typical of those obtained in a diversity of applications.

The problem with most of the standard algorithms is the manner in which measures are taken, especially as the necessary limits are approached. In particular, at the heart of most algorithms is a cover, or a measure of the area that the curve fills at some scale (ϵ). Fractal dimension is then obtained as an estimate of how this area varies with scale for a given curve. In light of this problem, then, we further proposed a new method for evaluating fractal dimension based not on coverings with disks and pixels, but rather with appropriately defined intervals. The resulting cover leads to a new class of algorithms yielding significantly more accurate estimates of fractal dimension. Our best algorithm—the variation method—is much more efficient than the others as well.

This paper is the first in a series of two, in which we both critiqued the standard algorithms and introduced the variation method. All analyses and experiments were done in one dimension, however, and in the companion paper[10] we show how to generalize the variation method to higher dimensions. The result is then a reliable and efficient algorithm for estimating the fractal dimension of surfaces.

ACKNOWLEDGMENTS

The authors wish to thank D. Wehbi for useful discussions and Lee Iverson for LISP machine support. This research was supported by the Natural Sciences and Engineering Research Council of Canada (NSERC) Grant No. A4470 for one of us (S.W.Z.); another (B.D.) is also supported in part by NSERC.

[1]P. Pfeifer, Appl. Surf. Sci. **18**, 146 (1984).
[2]J. P. Rigaut, J. Microsc. (Oxford) **133**, 41 (1984).
[3]B. H. Kaye, Powder Technol. **21**, 1 (1978).
[4]N. N. Clark, Powder Technol. **46**, 45 (1986).
[5]M. F. Goodchild, Math. Geo. **12**, 85 (1980).
[6]B. B. Mandelbrot, D. E. Passoja, and A. J. Paullay, Nature (London) **308**, 721 (1984).
[7]A. P. Pentland, IEEE Trans. Pattern Anal. Mach. Intell. **6**, 661 (1984).
[8]S. Peleg, J. Naor, R. Hartley, and D. Avnir, IEEE Trans. Pattern Analy. Mach. Intell. **6**, 518 (1984).
[9]J. Serra, *Image Analysis and Mathematical Morphology* (Academic, London, 1982).
[10]B. Dubuc, S. W. Zucker, C. Tricot, J. F. Quiniou, and D. Wehbi, McGill Research Center for Intelligent Machines Technical Report No. CIM-87-19, 1988 (unpublished).
[11]C. Tricot, J. F. Quiniou, D. Wehbi, C. Roques-Carmes, and B. Dubuc, Rev. Phys. Appl. **23**, 111 (1988).
[12]G. Bouligand, Bull. Sci. Math. **2**, 185 (1929).
[13]B. B. Mandelbrot, *The Fractal Geometry of Nature* (Freeman, San Francisco, 1982).
[14]B. B. Mandelbrot, Phys. Scr. **32**, 257 (1985).
[15]C. McMullen, Nagoya Math. J. **96**, 1 (1984).
[16]B. B. Mandelbrot and J. W. VanNess, SIAM (Soc. Ind. Appl. Math.) Rev. **10**, 422 (1968).
[17]R. F. Voss, in *Fundamental Algorithms for Computer Graphics,* edited by R. A. Earnshaw (Springer-Verlag, New York, 1985), pp. 805–835.
[18]S. Dubuc and Z. Elqortobi, Cah. Cent. Etud. R. Oper. Vol. (to be published).
[19]C. Tricot, Gaz. Sci. Math. Que. **10**, 3 (1986).
[20]M. V. Berry, and Z. V. Lewis, Proc. R. Soc. London, Ser. A **370**, 459 (1980).
[21]C. Roques-Carmes, D. Wehbi, J. F. Quiniou, and C. Tricot, in Extended Abstracts of the 1986 MRS Fall Meeting, Boston, 1986, edited by D. W. Schaefer, R. Laibowitz, B. B. Mandelbrot, and S. H. Lin (Materials Research Society, Pittsburg, 1986), pp. 112–114.
[22]G. Borgefors, Comput. Vision, Graphics and Image Processing **27**, 321 (1984).
[23]R. F. Voss, in *Scaling Phenomena in Disordered Systems,* Vol. 133 of *NATO Advanced Study Institute, Series B: Physics,* edited by Roger Pynn and Arne Skjeltorp (Plenum, New York, 1985), pp. 1–11.
[24]C. Tricot, J. Chim. Phys. **85**, 379 (1988).
[25]F. M. Dekking and P. J. Van Otterloo, IEEE Trans. Syst. Man Cybern. **16**, 395 (1986).
[26]W. Rudin, *Real and Complex Analysis* (McGraw-Hill, New York, 1974).
[27]C. Tricot, Université de Montréal Technical Report No. CRM-1532, 1988 (unpublished).
[28]J. F. Quiniou (unpublished).
[29]B. Dubuc, M. Eng. thesis, McGill University, Montréal, 1988.

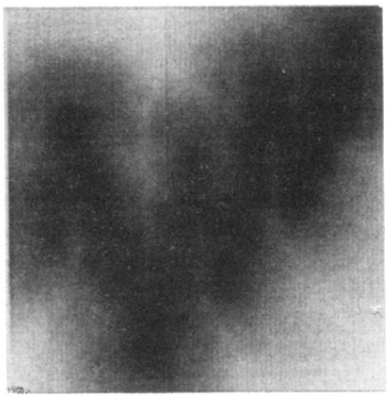

FIG. 5. Distance transform applied to the Kiesswetter curve of Fig. 4(b). The distance is displayed as a gray level intensity: dark corresponds to points close to the object and bright to points that are far away.